Ultrasonics Sonochemistry 72 (2021) 105454

Contents lists available at ScienceDirect

Ultrasonics Sonochemistry

journal homepage: www.elsevier.com/locate/ultson

Ultrasound assisted synthesis of highly active nanoflower-like $CoMoS_4$ electrocatalyst for oxygen and hydrogen evolution reactions

A.A. Yadav [a,*], Y.M. Hunge [b], Seok-Won Kang [a,*]

[a] Department of Automotive Engineering, Yeungnam University, 280 Daehak-ro, Gyeongsan, Gyeongbuk 38541, Republic of Korea
[b] Photocatalysis International Research Center, Tokyo University of Science, Yazamaki, Noda 278-8510, Chiba, Japan

ARTICLE INFO

Keywords:
$CoMoS_4$
Hydrogen evolution
Oxygen evolution
Overall water splitting

ABSTRACT

Rapid technological development requires sustainable, pure, and clean energy systems, such as hydrogen energy. It is difficult to fabricate efficient, highly active, and inexpensive electrocatalysts for the overall water splitting reaction: the oxygen evolution reaction (OER) and hydrogen evolution reaction (HER). The present research work deals with a simple hydrothermal synthesis route assisted with ultrasound that was used to fabricate a 3D nanoflower-like porous $CoMoS_4$ electrocatalyst. A symmetric electrolyzer cell was fabricated using a $CoMoS_4$ electrode as both the anode and cathode, with a cell voltage of 1.51 V, to obtain a current density of 10 mA/cm^2. Low overpotentials were observed for the $CoMoS_4$ electrode (250 mV for OER and 141 mV for HER) at a current density of 10 mA/cm^2.

1. Introduction

In recent years, excessive use of non-renewable energy sources has led to environmental pollution; therefore, there is a need to develop sustainable and clean energy sources. Hydrogen is considered a promising alternative to non-renewable energy sources because of its high energy density, abundant resources, and non-polluting nature [1,2]. Electrochemical water splitting is considered a good and clean technology for harvesting pure hydrogen. It consists of two half-cell reactions; one taking place at the cathode (hydrogen evolution reaction (HER)) and the other at the anode (oxygen evolution reaction (OER)) [3]. To complete the overall water splitting reaction, an overpotential is required potential to overcome the barriers of solution resistance, electrolyte/electrode interface resistance, and activation energy [4,5]. To minimize overpotential, there is a need to develop electrolytic cells with good active electrode materials. Currently, Ru and Mn-based electrode materials are used as active catalysts in the OER, and Pt-based materials in the HER. The main drawback of these materials is their high cost and low reversibility [5–7]. Consequently, earth-abundant electrocatalysts are required for the water splitting reactions. In addition, use of multifunctional electrocatalyst material for complete water splitting in similar electrolytes is more efficient. Therefore, it is essential to fabricate effective and active electrocatalysts for the overall water splitting reaction.

Recently, ternary metal sulfides have increasing attention owing to their outstanding properties such as high electrical conductivity, multiple oxidation states, and use in various applications, including electronics, catalysis, and energy storage [8–14]. A literature review shows that $CoSe_2$ [8], CoS/MoS_2 [9], Ni_3S_2/NF [10], and NiCoP [11] have been used as multifunctional materials for the water splitting reactions. $CoMoS_4$ has been considered a potential candidate material. Compared to binary sulfides (MoS_2 and CoS_2), the electrocatalyst $CoMoS_4$ exhibits multiple oxidation states; therefore it may provide large number of active sites for redox reactions and a modified electronic structure, which can help enhance the electrochemical properties [15]. Also, the active sites of the $CoMoS_4$ electrode can be enhanced using engineered morphology. The morphology of electrode is modified using ultrasonic treatment [16]. The use of ultrasound during solution mixing process increases mass and heat transfer. The nano size mono or bi-metallic electrodes are synthesized using ultrasound in absence or presence of surfactants and alcohol. The formation of nano-metallics is attributed to free radicals ($H^{\cdot}$ and $OH^{\cdot}$) generated by water in the process of sonolysis caused by cavitation. The nano-metallic size depends on the ultrasonic frequency, time, atmospheric gas, alcohol and surfactant. This effect mainly caused due to formation of high energy bubbles, which generates high velocity microjets of liquid (~200 m/s) [17]. Directly grown nanostructured morphology on a conducting substrate may provide more binder-free active sites than a powder-formed electrode, and may

* Corresponding authors.
E-mail address: anujayadav5@gmail.com (A.A. Yadav), swkang@yu.ac.kr (S.-W. Kang).

https://doi.org/10.1016/j.ultsonch.2020.105454
Received 7 December 2020; Received in revised form 21 December 2020; Accepted 23 December 2020
Available online 27 December 2020

also improve gas and solution diffusion and reduce contact resistance [15]. There are few reports on the use of $CoMoS_4$ catalyst in the water splitting reaction. Sun et al. [16] fabricated an amorphous $CoMoS_4$ electrocatalyst for overall water splitting with overpotentials of 143 and 342 mV for the HER and OER, respectively, to generate a current density of 10 mA/cm^2. Ren et al. [19] prepared $CoMoS_4$ nanosheets on carbon cloth via a hydrothermal route and Co(OH)F as a mediator with an overpotential of 183 mV to generate a current density of 10 mA/cm^2 in 1.0 M phosphate buffer solution.

In this study, a 3D nanoflower-like $CoMoS_4$ electrode was fabricated using ultrasound assisted hydrothermal method. $CoMoS_4$ was directly grown on a nickel foam (NF) substrate. A $(NH_4)_2MoS_4$ precursor was synthesized and used for the fabrication of a 3D nanoflower-like $CoMoS_4$ electrocatalyst. Due to abundant active sites, low electrolyte contact resistance, and fast transfer of electrons, the $CoMoS_4$ electrode showed excellent electrocatalytic activity. For $CoMoS_4$ electrode, low overpotential value to generate 10 mA/cm^2 in 1.0 M KOH electrolyte is required for both HER and OER reactions. In addition, the porous structure of $CoMoS_4$ provides an ideal channel for electrolyte diffusion, which enhances the reaction kinetics of the catalyst and facilitates the release of the produced gas.

2. Methods and materials

2.1. Materials

Chemical reagents included $Co(NO_3)_2$, $(NH_4)_2Mo_7O_{24}$, KOH, $(NH_4)_2S$, H2PtCl6, carbon black , PVP, and RuO_2 were purchased from Sigma-Aldrich.

2.2. Synthesis of $CoMoS_4$/NF

To synthesize the $(NH_4)_2MoS_4$ precursor; 0.35 M $(NH_4)_2Mo_7O_{24}$ was prepared in 30 mL of double distilled water (DDW) and 15 mL of ammonia. Next, 8 wt.% of $(NH_4)_2S$ was added. The solution was mixed with continuous magnetic stirring and placed in a ultrasonic bath at a constant temperature of 70 °C for 2 h. The mixture was then cooled and allowed to crystallize at room temperature (RT) for 12 h. Then, the crystals were washed with ethanol and water several times and dried at room temperature. The following reaction takes place to form $(NH_4)_2MoS_4$ [2]:

$$(NH_4)_2Mo_7O_{24} + 8NH_3{\cdot}H_2O \rightarrow 7(NH_4)_2MoO_4 + 4H_2O \quad (1)$$

$$(NH_4)_2MoO_4 + 4(NH_4)_2S \rightarrow (NH_4)_2MoS_4 + 4NH_3 + H_2O \quad (2)$$

For the synthesis of the $CoMoS_4$/NF electrocatalyst, 1 M Co $(NO_3)_2{\cdot}6H_2O$ and $(NH_4)_2MoS_4$ were dissolved in 25 mL of DDW and to from uniform mixture solution was sonicated for 25 min ultrasonic probe sonicator (20 kHz), that was further transferred to a Teflon-lined autoclave. Literature shows various reports on the synthesis of nanostructures using ultrasound [20(a),20(b)].

The NF substrate was cleaned with acetone and immersed in the reaction mixture. The whole assembly was kept at a constant temperature of 120 °C for 4, 8, 12, and 16 h, and the samples were coded as CM-4, CM-8, CM-12, and CM-16, respectively. The deposited electrode was removed from the Teflon-lined autoclave and cleaned with DDW and ethyl alcohol. The reaction occurring during the process of $CoMoS_4$ electrode synthesis is as follows [20 (a)]:

$$Co(NO_3)_2 + (NH_4)_2MoS_4 \rightarrow CoMoS_4 + 2NH_4NO_3 \quad (3)$$

The structural, morphological, and electrochemical performance of the synthesized $CoMoS_4$/NF electrode were studied. Fig. 1 shows a schematic diagram of the synthesis of $CoMoS_4$/NF electrode.

The previously reported method was used for the fabrication of Pt/C electrode. In this method, pulsed galvanostatic electrodeposition and ultrasonication treatment with high power ultrasound (with frequency of 20 kHz) were used for fabrication of Pt/C electrode for comparison in case of HER study of $CoMoS_4$ [21(a),21 (b)].

2.3. Material characterization

X-ray diffraction (XRD, Rigaku, Japan, Cu Kα radiation) was employed to study the structure of the synthesized electrodes. The morphology and elemental distribution were observed using TEM and EDS (JEM-2010, Japan), respectively. The morphological profile was obtained using SEM (JEOL, Japan). The phase composition of the

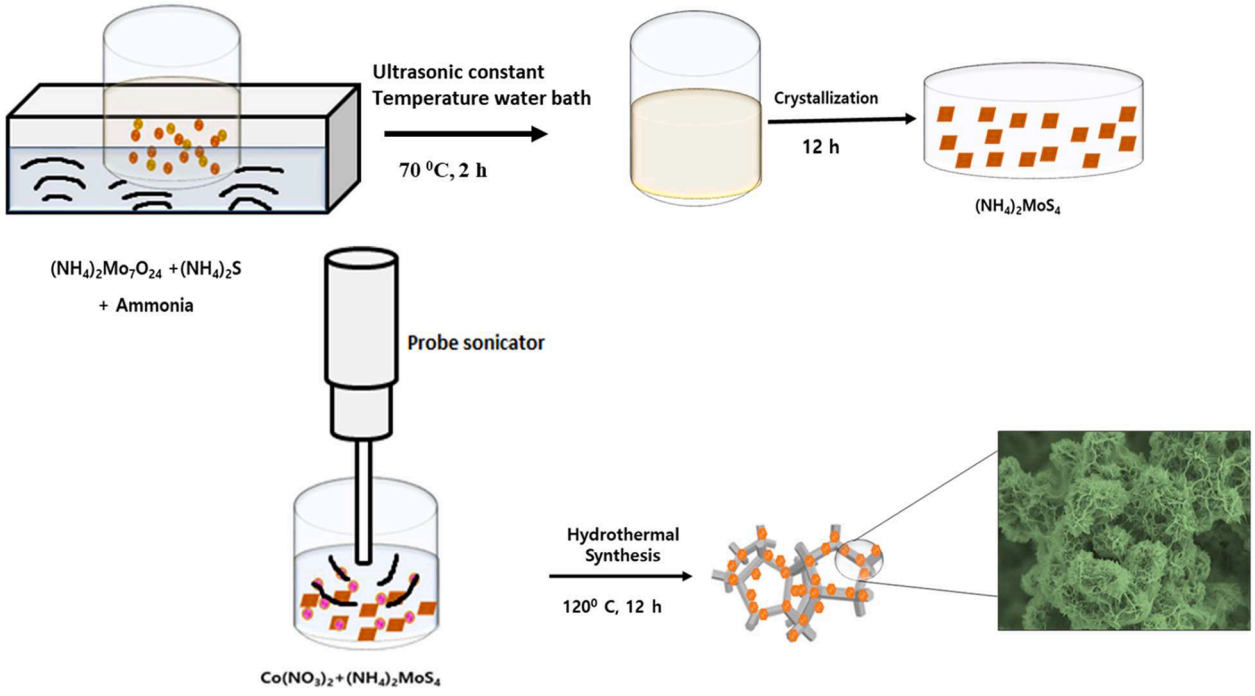

Fig. 1. Schematic diagram of the synthesis of porous 3D nanoflower-like $CoMoS_4$ on Ni foam.

synthesized electrode was confirmed by XPS (PHI 5300 ESCA). The surface area of the synthesized electrode was measured using the Brunauer-Emmett-Teller (BET) method.

2.4. Electrochemical measurements

The electrocatalytic properties of the synthesized electrodes were measured in a 1 M KOH electrolyte using a three-electrode system. The chemically synthesized electrodes were used as the working electrode, Ag/AgCl as the reference electrode, and a platinum electrode as the counter electrode. The OER and HER electrocatalytic properties were measured using a VersaSTAT3 instrument, Ametek, Japan. Polarization curves were measured via linear sweep voltammetry (LSV) curves at 2 mV/s (scan rate) in a 1 M KOH electrolyte. The potentials measured were calibrated with respect to the RHE using the following equation [22,23]:

$$E_{vs.RHE} = E_{vs.Agcl} + 0.059 \times pH + 0.197 \quad (4)$$

The overpotential (η) for the prepared current density was calculated using the following equation:

$$\eta = E_{vs.RHE} - 1.23\ V \quad (5)$$

Tafel slopes were measured using LSV polarization curves with plots of overpotential vs. log (*i*), given by the following equation:

$$\eta = a + blogi \quad (6)$$

where *a* is the exchange current density and *b* is the slope of the Tafel plot. The durability of the electrocatalyst was studied using a chronoamperometric study. The electrochemical double-layer capacitance (C_{dl}) is considered to be a measure of the electrochemically active surface area. Cyclic voltammetry (CV) curves were obtained in a non-Faradaic voltage window (0.1 V), and the current values obtained in this region are considered to be the double-layer current. This is explained by the following equation [23]:

$$i = \frac{dq}{dt} = \frac{d(C_{dl})}{dt} = C_{dl}\frac{d\varphi}{dt} + \varphi\frac{dC_{dl}}{dt} \quad (7)$$

where the charging current (*i*) is formed of two parts. The first part is due to the state of charge at the electrode/electrolyte interface and changes with potential (φ), and the other part is due to the change in C_{dl} with respect to the double-layer current. However, the voltage window is small because the charged state of the electric double layer is considered to remain constant, and the respective C_{dl} also remains constant with time. This means that equation (7) can be reduced to equation (8):

$$i = C_{dl}\frac{d\varphi}{dt} = C_{dl}v \quad (8)$$

where *v* is the scan rate. The electrochemically active surface area (ECSA) of the electrocatalyst was calculated using the following equation:

$$\mathrm{ECSA} = \frac{C_{dl}}{C_s} \quad (9)$$

where C_s is the specific capacitance of the sample. The roughness factor was calculated as follows:

$$\mathrm{RF} = \frac{\mathrm{ECSA}}{\mathrm{Geometric\ area}} \quad (10)$$

The geometric area of the electrocatalyst used was 1 cm^2. To determine the Faradaic efficiency, gas chromatography was used, which was then quantified and calibrated using a pressure sensor with an H-type electrocatalytic cell. Before starting the experiments, N_2 gas was passed through the solution for 30 min with continuous stirring. The theoretical quantity of O_2 and H_2 gas produced was measured using Faraday's law:

$$n = \frac{Q}{zF} \quad (11)$$

where *n* is the number of moles of the generated gas, *Q* is the number of coulombs passed over time, *F* is the Faraday constant (96480C/mol), and *z* is the number of electrons taking part in the OER and HER reactions (HER = 2, OER = 4).

3. Results and discussion

The XRD pattern for $CoMoS_4$ is shown in Fig. 2(a) and inset show the XRD pattern for $(NH_4)_2SO_4$. An absence of characteristic diffraction peaks was observed in the XRD pattern of $CoMoS_4$, which confirms its amorphous nature, matching with previous reports [18,24]. The formation of $(NH_4)_2SO_4$ was confirmed using JCPDS card No.48–1662 [1]. Therefore, Raman and XPS studies were performed to analyze the chemical species present on the surface of the electrode. Fig. 2(b) shows the Raman spectra for CM-4, CM-8, CM-12, and CM-16. The band observed at 931 cm^{-1} corresponds to symmetric broadening vibrations related to Mo-S, and bands at 812 and 856 cm^{-1} are associated with S-Mo-S (S asymmetric stretching mode). The bands at 365 and 404 cm^{-1} are related to Co-Mo-S, for the symmetric stretching mode and S out-of-plane vibration in the transverse plane, respectively. Thus, the formation of a 3D nanoflower-like amorphous $CoMoS_4$ electrode was confirmed using Raman spectroscopy [15].

Fig. 2(c) shows the XPS survey scan spectrum for the amorphous CM-12 sample, which confirms the presence of Co, Mo, and S elements and no other impurity elements. The high-resolution Co 2p XPS spectrum splits into two peaks due to spin–orbit coupling (Fig. 2(d)). The peaks observed at 797.5 and 781.5 eV belong to the Co $2p_{1/2}$ and Co $2p_{3/2}$ core levels, respectively, which confirms that Co occurs in the +2 oxidation state [25]. The other two smaller peaks detected at 793.9 and 778.6 eV are correspond to the presence of Co^{3+} oxidation state. In the case of Mo 3d spectrum (Fig. 2(e)), two peaks located at binding energies of 231.4 and 228.3 eV are associated with the $3d_{3/2}$ and $3d_{5/2}$ states, respectively. They correspond to the Mo^{4+} oxidation state. The peak observed at 225.5 eV is associated with the S 2 s core level, which is correlated with the Co-S bond [26]. The S 2p high-resolution XPS spectrum shown in Fig. 2(f) shows that the peaks located at binding energies of 161.2 and 162.8 eV correspond to S $2p_{1/2}$ of the Co-S bond. The peaks located at 162.1 and 163.4 eV are attributed to Mo-S bonds [18,27].

SEM images for CM-4, CM-8, CM-12, and CM-16 samples are shown in Fig. 3(a-d). An internally connected nanosheet-like morphology is observed for CM-4 and CM-8 (Fig. 3(a) and (b)). As the deposition time interval increases to 12 h in CM-12, the nanosheets self-assemble into a porous 3D nanoflower-like structure, and these nanoflowers are interconnected by nanosheets. The nanosheets are also connected with the NF, which helps the charge transfer process from the active material (CM-12) to the NF current collector (Fig. 3(c)). The highly porous nature of the CM-12 electrode helps to reduce the diffusion path for electrolyte ions in the electrode material, which may help to improve electrocatalytic performance. Fig. 3(d) displays the CM-16 electrode, showing agglomeration and peeling of the active material from the NF substrate. The TEM image in Fig. 3(e) confirms that the amorphous nature of the CM −12 electrocatalyst consists of a 3D-nanoflower-like structure. This highly porous structure is useful for the diffusion of KOH electrolyte. The amorphous nature of the CM-12 electrode is supported by the SAED pattern shown in Fig. 3(f) [1].

Absorption and desorption isotherms were obtained to determine the surface area and pore size distribution using BET characterization, and the results are presented in Fig. 4. The isotherms observed for the CM-4, CM-8, CM-12, and CM-16 electrodes (Fig. 4 (a-d)) are of type IV. According to the guidelines of the International Union of Pure and Applied Chemistry (IUPAC), all electrodes are mesoporous in nature [28]. The amount of N_2 absorption rapidly increases when the pressure reaches 1

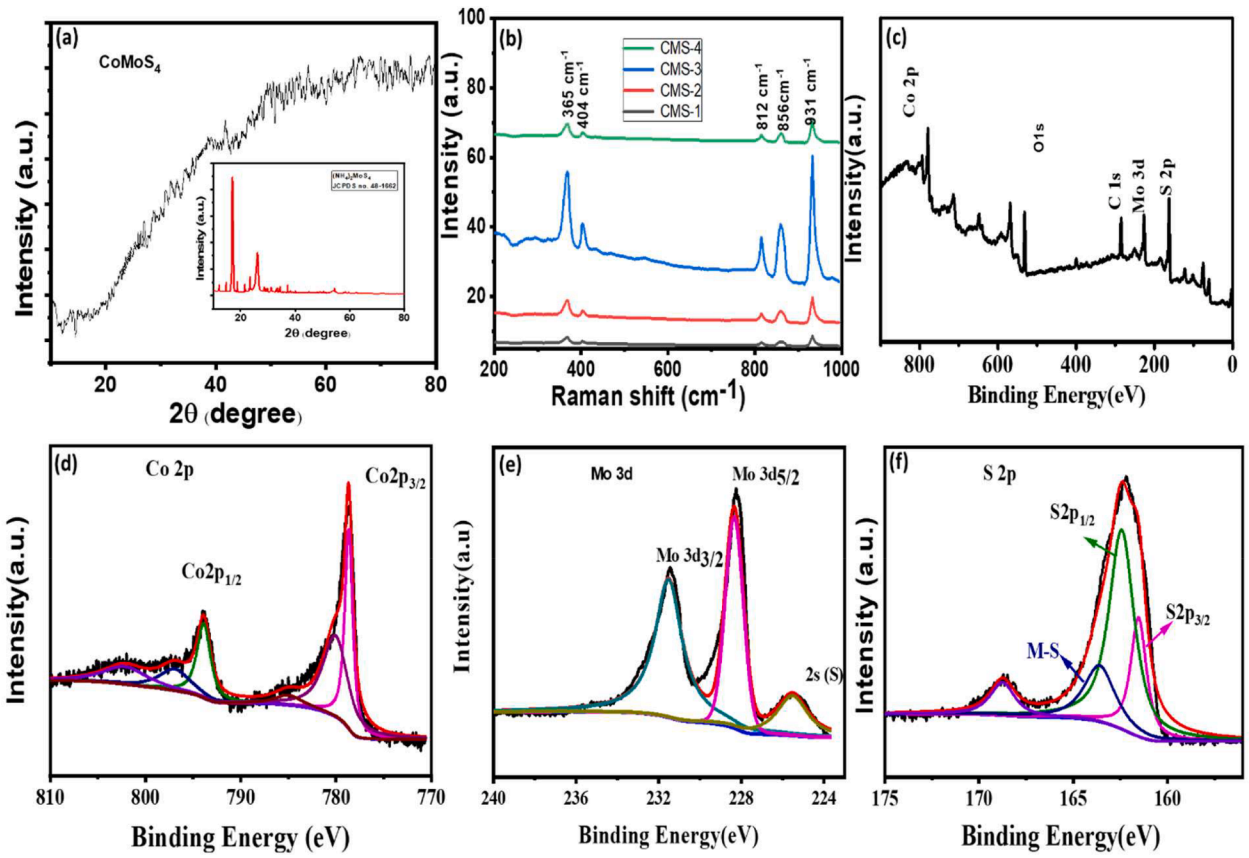

Fig. 2. (a) XRD pattern for $CoMoS_4$ and inset show XRD pattern for $(NH_4)_2SO_4$, (b) Raman spectra for CM-4, CM-8, CM-12, and CM-16 electrocatalysts. High resolution XPS spectra (c) survey spectra, (d) Co 2p, (e) Mo 3d, and (f) S 2p.

atm, which is related to the mesoporous nature of the electrodes [29]. The surface areas calculated for the CM-4, CM-8, CM-12, and CM-16 electrodes were 51.07, 54.74, 62.68, and 52.83 m^2/g, respectively. Fig. 4(e, f, g, and h) shows the pore size distribution in these electrodes, providing evidence of the mesoporous nature of the electrodes, which may improve their electrochemical properties by allowing penetration of the electrolyte and therefore, good contact at the electrolyte–electrode interface [30].

4. Overall water splitting study

4.1. Oxygen evolution activity (OER)

An electrode with an amorphous structure has more active sites than a crystalline one because of unsaturated vacancies on its surface; therefore, $CoMoS_4$ is a potential electrocatalyst. The electrolyte was initially saturated with O_2 to secure a reversible oxygen potential at 2 mV/s using three electrodes at room temperature. Fig. 5(a) displays polarization curves for CM-4, CM-8, CM-12, and CM-16 electrodes at a sweep rate of 2 mV/s, and the overpotential values obtained were 288, 274, 250, and 278 mV, respectively. From this study, it is clear that Co and Mo metal ions in a single electrocatalyst enhance the OER performance [30]. An important parameter in the OER study is the Tafel slope. The CM-12 electrocatalyst delivered a current density of 10 mA/cm^2 at a low overpotential of 250 mV and a Tafel slope of 51.9 mV/dec (Fig. 5 (b)). Thus, the low values observed for the overpotential and the Tafel slope confirm that porous 3D-nanoflower-like CM-12 electrocatalysts can enhance the OER catalytic activity [18,31]. Fig. 5(c) shows values of the Tafel slope for CM-4, CM-8, CM-12, and CM-16 electrodes, respectively. A durability study was conducted using chronoamperometry, as shown in Fig. 5(d). The current density remained unchanged during a 12 h durability test. Thus, improved stability, charge transport resistance, and contact resistance are important factors in the study of the OER activity of CM-12 [32–34]. LSV curves for the CM-12 electrocatalyst were obtained for the 1st and 3000th CV cycles. Fig. 5(e) shows that there is a negligible difference between the two, recorded at 2 mV/s in 1 M KOH electrolyte, and the overpotential increased from 250 to 254 mV. The Faradaic efficiency of the evolution of O_2 gas in the OER study for the CM-12 electrocatalyst was calculated using both experimental and theoretical methods. Galvanostatic measurements were used in this study. The CM-12 electrocatalyst maintained a constant current density of 10 mA/cm^2 for 12 h in a 1 M KOH solution. The amount of O_2 evolved was calculated theoretically using equation (7) and experimentally using gas chromatography. A comparison of the experimental and theoretical results shows that a Faradaic efficiency of 98% was observed during the OER study (Fig. 5(f)). This confirms that nearly all charges are utilized for the oxidation of water into oxygen [35–36].

Fig. 6(a) presents a Nyquist plot for the CM-12 sample in 1 M KOH electrolyte at 1.5 V. The solution resistance (R_s) and the charge transfer resistance (R_{ct}) are related to the semicircles observed in the low- and high-frequency regions [36]. The observed value of R_s is 0.7 Ω for the CM-12 sample, showing that the porous CM-12 electrocatalyst has a low impedance and fast charge transfer properties. The electrochemical surface area (ESCA) and roughness are other important factors affecting the electrochemical performance [37–39]. Determination of the ESCA is based on the value of C_{dl}, which can be measured by CV study in aqueous 1 M KOH electrolyte. The CV curves were observed within a non-Faradaic voltage window in the range + 0.61 to + 0.71 vs RHE at various scan rates from 5 to 80 mV/s, as shown in Fig. 6(b). It is difficult to determine the precise value of the surface area of an electrocatalyst, but the relative value of the surface area can be estimated. The C_{dl} in the case of CM-12 is 19.89 mF/cm^2. Fig. 6(c) shows the cathodic (i_c) and

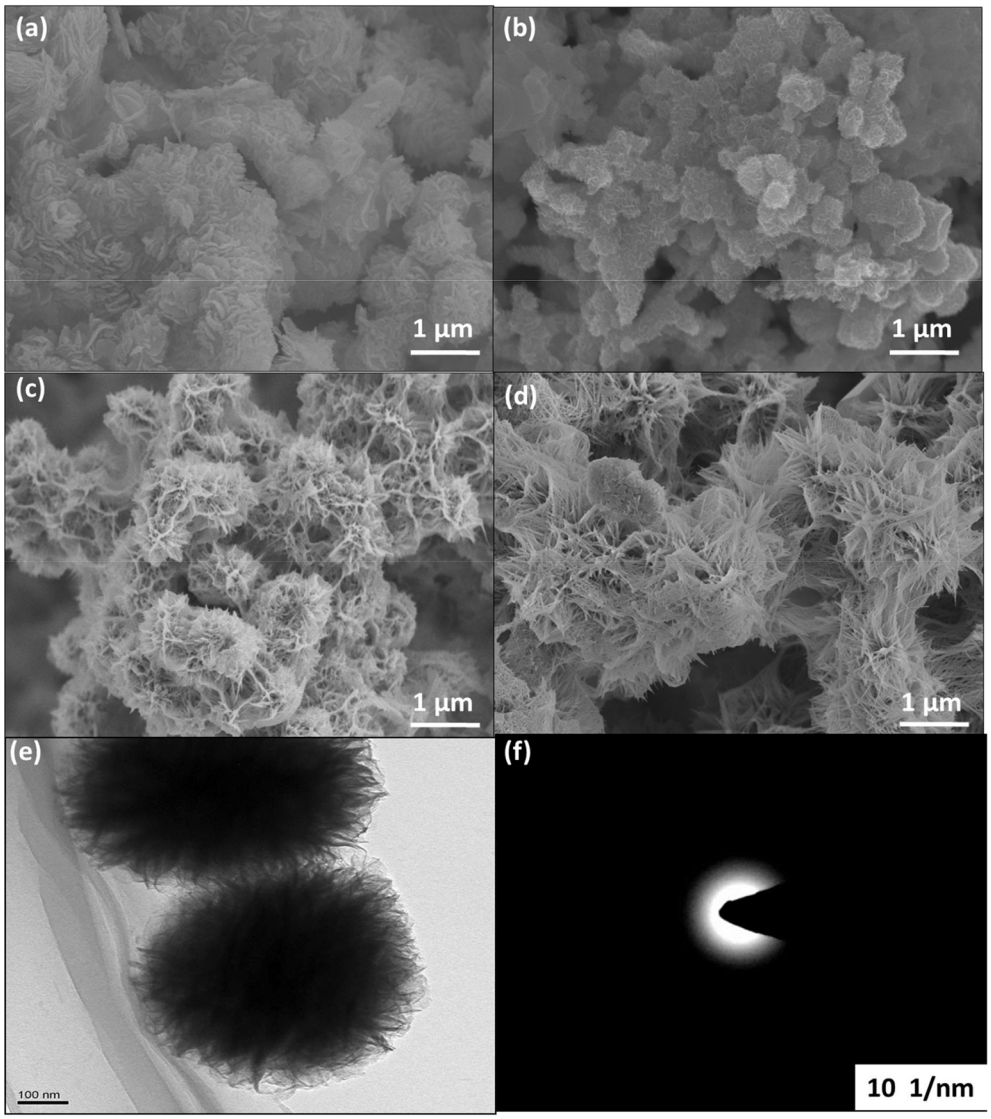

Fig. 3. SEM images of $CoMoS_4$ deposited for different time intervals (a) CM-4, (b) CM-8, (c) CM-12, and (d) CM-16. (e) TEM image, and (d) selected electron diffraction pattern for CM-12.

anodic (i_a) current densities versus scan rates. The ESCA is directly proportional to C_{dl}; therefore, C_{dl} suggests that the CM-12 electrocatalyst has a larger surface area along with a high roughness factor. Thus, the large number of active sites is partly responsible for its superior performance.

4.2. Hydrogen evolution activity (HER)

HER studies of CM-4, CM-8, CM-12, and CM-16 electrodes were performed in aqueous 1 M KOH using LSV techniques. The polarization curves observed for these electrodes are shown in Fig. 7(a). Overpotential values of 164, 157, 141, and 161 mV were calculated for these electrodes, respectively. The overpotential required for the CM-12 electrocatalyst was 141 mV to achieve 10 mA/cm^2. This result shows similar behavior to that of the OER study. The NF had a larger overpotential (260 mV) in the alkaline medium. Tafel plots for CM-4, CM-8, CM-12, CM-16, Pt/C, and NF are shown in Fig. 7(b) and their slopes of 104.8, 86.5, 60.1, 104.8, 94.8, 59.2, and 184.4 mV/dec, respectively, are shown in Fig. 7(c). It is known that Tafel slope values reflect the electric transport properties of the catalyst, with a low value of Tafel slope and high electric conductivity observed in the catalyst [1]. A study of the HER durability and stability for the CM-12 electrocatalyst was carried out using LSV curves and chronoamperometry. Fig. 7(d) shows that only slight degradation after 3,000 CV cycles is observed, confirming that the CM-12 electrocatalyst is highly stable for both the OER and HER activities. The durability study of CM-12 performed at −0.15 V vs. RHE for 12 h is presented in Fig. 7(e), and no obvious changes are found. Faradaic efficiency for HER activity was similar to that for the OER. From Fig. 7(f), it can be seen that the experimental and theoretical values of the calculated H_2 gas evolved were similar. The Faradaic efficiency of the HER activity calculated for the $CoMoS_4$ electrocatalyst is 99% [38,39].

4.3. Two-electrode water electrolyzer studies

The OER and HER activity studies show that the CM-12 electrode has high stability, durability, and activity for overall water splitting. To produce pure hydrogen and to study complete water splitting, a two-electrode electrolyzer system was fabricated. $CoMoS_4$/NF was used as both the anode and cathode ($CoMoS_4$/NF//$CoMoS_4$/NF) electrocatalyst in 1 M KOH electrolyte, and the area of each electrode was 1 cm^2.

LSV curves for electrolysis with $CoMoS_4$/NF//$CoMoS_4$/NF are shown in Fig. 8(a), which show that a current density of 10 mA/cm^2 is required in order to reach 1.51 V. Compared with recently reported materials, as

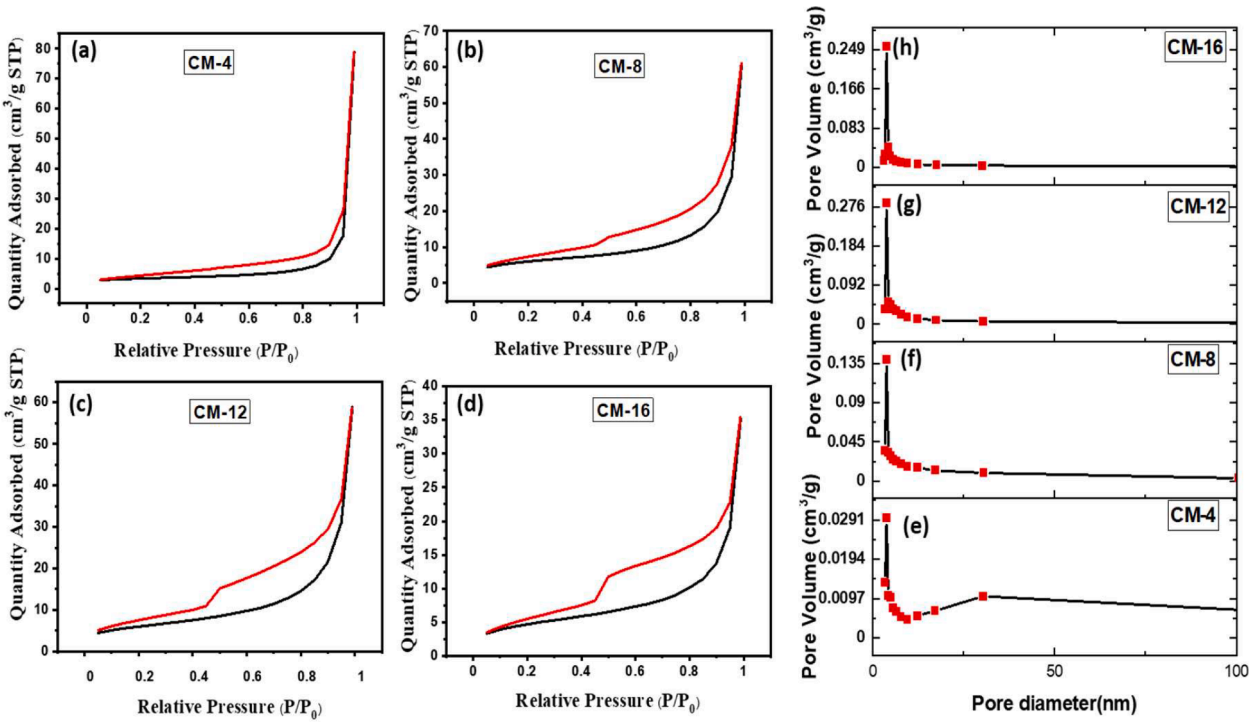

Fig. 4. (a, b, c, and d) BET surface area measured from nitrogen adsorption–desorption isotherms for CM-4, CM-8, CM-12, and CM-16, respectively; (e, f, g and h) pore size distribution for CM-4, CM-8, CM-12, and CM-16, respectively.

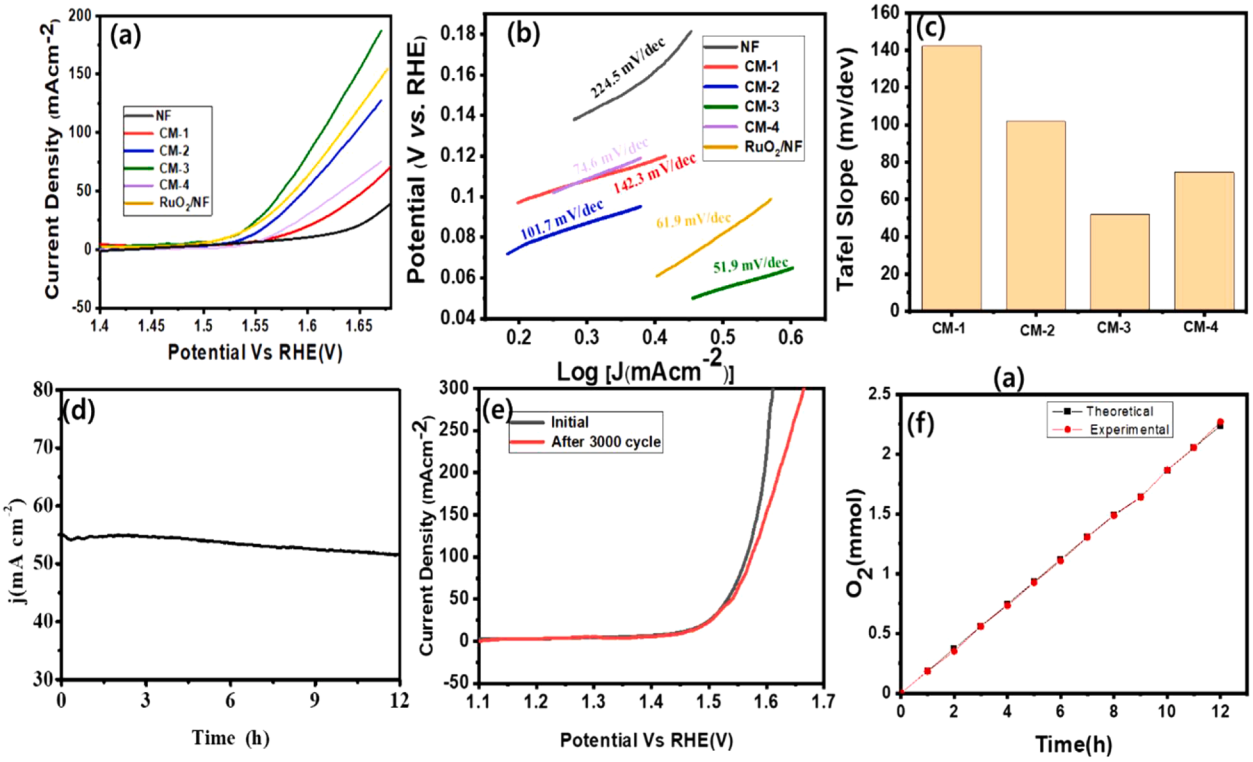

Fig. 5. (a) OER polarization curves for CM-4, CM-8, CM-12, and CM-16; (b) Tafel plots for CM-4, CM-8, CM-12, CM-16, RuO_2, and NF, in 1 M KOH, (c) the variation of Tafel slope for CM-4, CM-8, CM-12, and CM-16, (d) stability for 3000th cycle and, (e) durability study by chronoamperometry curves for the CM-12, (f) the amount of theoretically calculated (red line) and experimentally measured oxygen versus time for CM-12 at 10 mA/cm^2 for 12 h. (For interpretation of the references to colour in this figure legend, the reader is referred to the web version of this article.)

shown in Table 1, the water splitting cell voltage required for $CoMoS_4$/NF//$CoMoS_4$/NF shows superior performance [40,41]. Fig. 8(b) shows a stability study for $CoMoS_4$/NF//$CoMoS_4$/NF. This electrocatalyst shows high stability for 12 h with little loss of active material. To study the mechanism of electrocatalytic reactions for the OER and HER reactions, it is important to understand the surface behavior of electrocatalysts. In

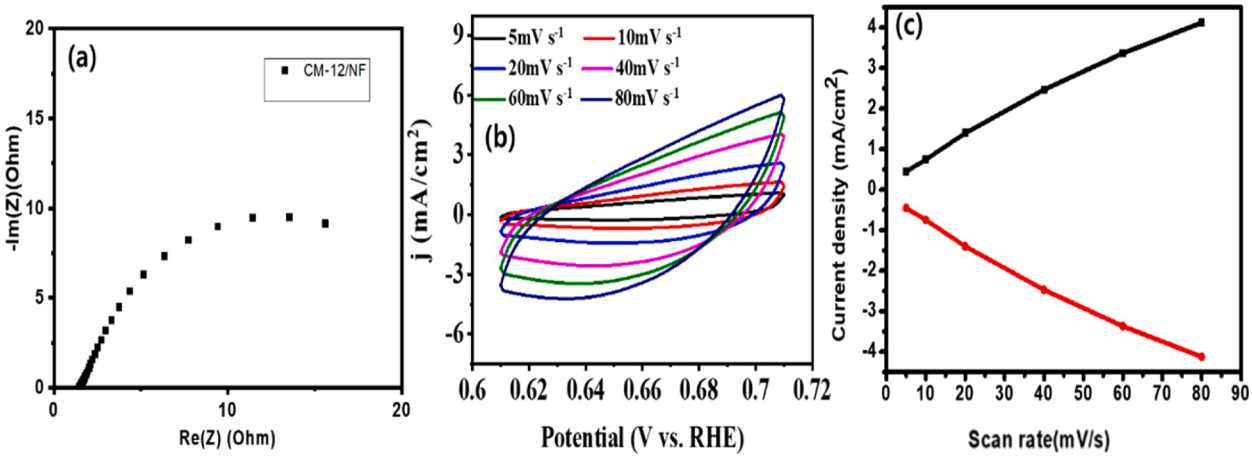

Fig. 6. (a) EIS spectra of CM-12, (b) cyclic voltammograms for CM-12, (c) The capacitive currents vs. RHE with a scan rate of in 1 M KOH.

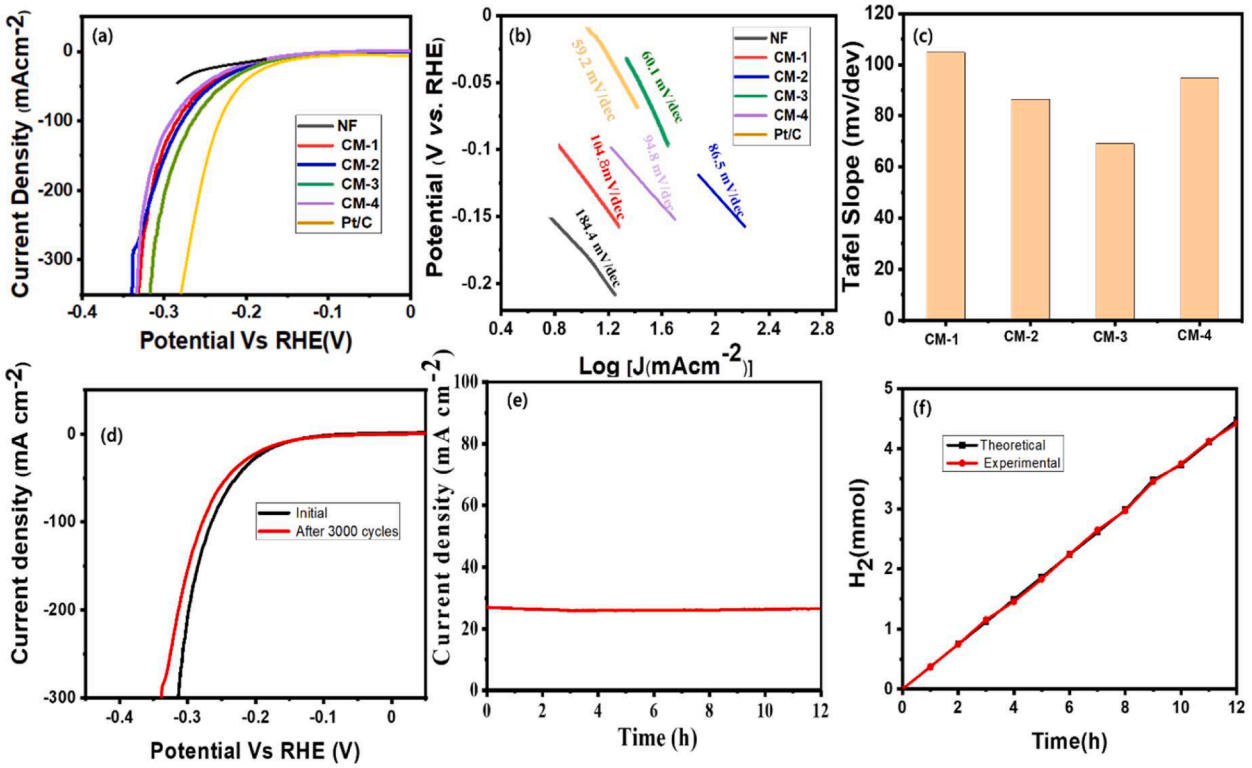

Fig. 7. (a) HER polarization curves, (b) the corresponding Tafel plots for CM-4, CM-8, CM-12, CM-16, Pt/C and NF in 1 M H_2-saturated KOH at scan rate 2 mV/s (c) variation of Tafel slope for CM-4, CM-8, CM-12, and CM-16 (d) stability for 3000th cycle and (e) durability study by chronoamperometry curves for the CM-12, (f) the amount of theoretically calculated (red line) and experimentally measured (black line) hydrogen versus time for CM-12 at 10 mA/cm^2 for 12 h. (For interpretation of the references to colour in this figure legend, the reader is referred to the web version of this article.)

the case of the OER, the $CoMoS_4$/NF electrocatalyst has an amorphous crystal structure, and its oxidation states, such as Co^{+3} and Mo^{+3}, result in large defects in the electrocatalyst, which allow the adsorption of reactant species, improving its catalytic activity [42]. The HER mechanism in alkaline medium is mainly based on the charge transfer process and is divided into three steps. In the Volmer step, protons (H^+) are adsorbed at electrochemically active sites present on the surface of the electrocatalyst. In the Heyrovsky step, the adsorbed hydrogen and another H^+ from the water molecule are coupled and H_2 evolves. In another proposed step, the Tafel step, two adsorbed hydrogen atoms are combined to form H_2. Thus, the HER process follows a mechanism of either (1) Volmer-Heyrovsky, or (2) Volmer-Tafel. According to the literature, the type of mechanism can be determined from the Tafel slope values. The Tafel slope obtained for $CoMoS_4$/NF was 53.4 mV/dec, confirming that $CoMoS_4$/NF has a Volmer-Heyrovsky mechanism, where the Heyrovsky step is considered to be the rate-determining step [23]. Table 1 shows a recently reported metal electrocatalysts for the complete water splitting reaction with HER and OER.

5. Conclusions

In this study, highly porous 3D-nanoflower-like $CoMoS_4$/NF electrodes were synthesized using a hydrothermal approach for various deposition times. The porous nanoflower-like structure provides a high number of active sites for the reaction because it acts as a multifunctional electrocatalyst for the HER and OER reactions in strong alkaline

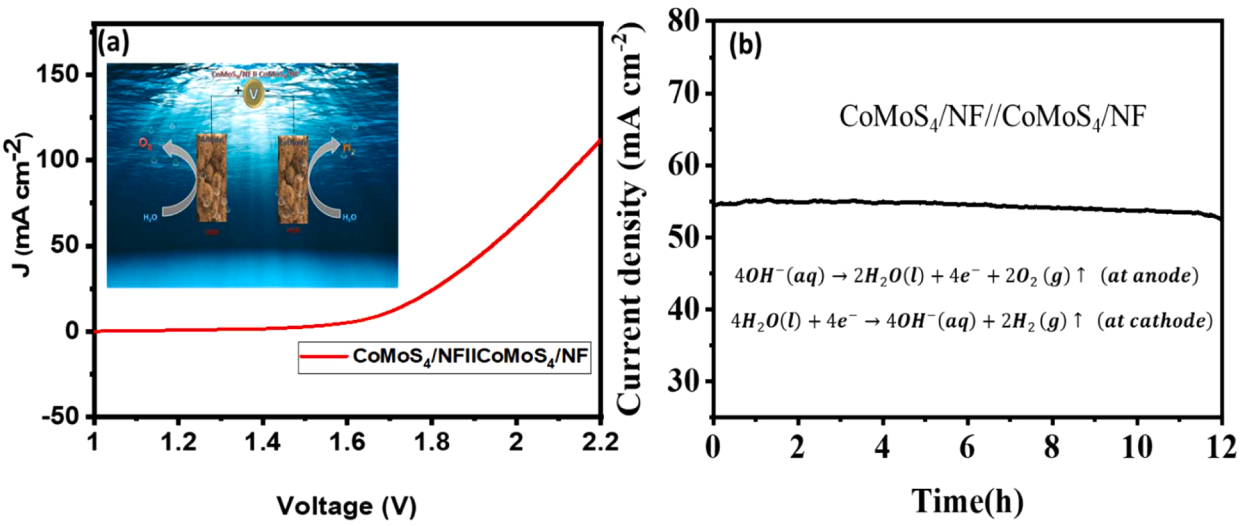

Fig. 8. (a) Polarization curves for $CoMoS_4$/NF//$CoMoS_4$/NF in 1 M KOH at 2 mV/s at room temperature. Inset: the overall water splitting cell. (b) Chronoamperometry durability test of two-electrode setup ($CoMoS_4$/NF//$CoMoS_4$/NF) at a constant current density of 10 mA/cm^2 over 12 h.

Table 1
The recently used non-precious metal electrocatalysts for OER, HER, and overall water splitting mainly in alkaline media.

Catalyst	OER		HER		Overall water splitting		Electrolyte	Reference
	j (mA/cm^2)	Overpotential (mV)	j (mA/cm^2)	Overpotential (mV)	j(mA /cm^2)	Potential (V)		
$CoMoS_4$/CC	10	342	10	143	10	1.72	1 M KOH	[18]
NiCo/$NiCo_2S_4$/NiCo/ NF	10	278	10	132	10	1.55	1 M KOH	[24]
$NiCo_2S_4$@NiFe LDH	60	201	10	200	10	1.6	1 M KOH	[43]
CoFe LDH-F	10	255	10	166	10	1.63	1 M KOH	[2]
$CoMoS_4$NS/ CC	–	–	10	183	–	–	1 M phosphate buffer	[19]
$CoMoS_4$/ Ni_3S_2	10	200	10	158	10	1.568	1 M KOH	[39]
$CoMoS_4$/NF	–	–	10	143	–	–	0.5 M H_2SO_4 or 1 M NaOH	[44]
$CoMoS_4$/NF	10	250	10	141	10	1.53	1 M KOH	[Present work]

media at low overpotentials with high stability and durability. An electrolyzer cell using nanoflower-like $CoMoS_4$ for both anode and cathode produced a current density of 10 mA/cm^2 at a cell voltage of 1.51 V. Thus, the engineered 3D-nanoflower-like porous $CoMoS_4$/NF electrode may be a potential candidate for overall water splitting.

CRediT authorship contribution statement

A.A. Yadav: Conceptualization, Investigation, Writing - original draft. **Y.M. Hunge:** Methodology, Investigation, Writing - original draft. **Seok-Won Kang:** Supervision, Writing - review & editing.

Declaration of Competing Interest

The authors declare that they have no known competing financial interests or personal relationships that could have appeared to influence the work reported in this paper.

Acknowledgment

This work was supported by the National Research Foundation of Korea (NRF) grant funded by the Korea government (MSIT) (No. NRF-2019R1A5A8080290).

References

[1] X. Xu, Q. Liu, L. Liang, H. Gu, Y. Zhao, X. Xing, X. Zhang, Y. Hu, Well-designed nanosheet-constructed porous $CoMoS_4$ arrays for ultrahigh-performance supercapacitors, Ceram. Int. 46 (4) (2020) 4878–4888, https://doi.org/10.1016/j.ceramint.2019.10.224.

[2] P.F. Liu, S. Yang, B.o. Zhang, H.G. Yang, Defect-rich ultrathin cobalt–iron layered double hydroxide for electrochemical overall water splitting, ACS Appl. Mater. Interfaces 8 (50) (2016) 34474–34481, https://doi.org/10.1021/acsami.6b12803.s002.

[3] Y. Pei, Y. Yang, F. Zhang, P. Dong, R. Baines, Y. Ge, H. Chu, P.M. Ajayan, J. Shen, M. Ye, Controlled electrodeposition synthesis of Co-Ni-P film as a flexible and inxpensive electrode for efficient overall water splitting, Appl. Mater. Interfaces 9 (2017) 31887–31896.

[4] X. Zou, Y. Zhang, Noble metal-free hydrogen evolution catalyst for water splitting, Chem. Soc. Rev. 44 (2015) 5148–5180.

[5] A. Sivanantham, P. Ganesan, S. Shanmugam, Hierarchical $NiCo_2S_4$ nanowire arrays supported on Ni foam: an efficient and durable bifunctional electrocatalyst for oxygene and hydrogene evolution reactions, Adv. Funct. Mater. 26 (2016) 4661–4672.

[6] X. Lu, W.-L. Yim, B.H.R. Suryanto, C. Zhao, Electrocatalytic oxygen evolution at surface-oxidized multiwall carbon nanotubes, J. Am. Chem. Soc. 137 (8) (2015) 2901–2907, https://doi.org/10.1021/ja509879r.

[7] J. Wang, W. Cui, Q. Liu, Z. Xing, A.M. Asiri, X. Sun, Recent progress in cobalt-based heterogeneous catalyst for electrochemical water splitting, Adv. Mater. 28 (2016) 215–230.

[8] I.H. Kwak, H.S. Im, D.M. Jang, Y.W. Kim, K. Park, Y.R. Lim, E.H. Cha, J. Park, $CoSe_2$ and $NiSe_2$ nanocrystals as superior bifunctional catalyst for electrochemical and photoelectrochemical water splitting, ACS Appl. Mater. Interfaces 8 (2016) 5327–5334.

[9] H. Zhu, J. Zhang, R.Y. Zhang, M. Du, Q. Wang, G. Gao, J. Wu, G. Wu, M. Zhang, B. Liu, J. Yao, X. Zhang, When cubic sulfide meets layered molybdenum disulfide: a core–shell system toward synergetic electrocatalytic water splitting, Adv. Mater. 27 (2015) 4752–4759.

[10] L.-L. Feng, G. Yu, Y. Wu, G.-D. Li, H. Li, Y. Sun, T. Asefa, W. Chen, X. Zou, High-index faceated Ni_3S_2 nanosheet arrays as highly active and ultrasatble electrocatalysts for water splitting, J. Am. Chem. Soc. 137 (2015) 14023–14026.

[11] H. Gu, W. Fan, T. Liu, Phosphrous- doped $NiCo_2S_4$ nanocrystals grown on electrospun carbon nanofibers as ultra –efficient electrocatayst for the hydrogen evolution reaction, Nanoscale 2 (2017) 277–283.

[12] Y. Zhou, H. Xiao, S. Zhang, Y. Li, S. Wang, Z. Wang, C. An, J. Zhang, Interlayer expanded lamellar CoSe 2 on carbon paper as highly efficient and stable overall water splitting electrodes, Electrochim. Acta 241 (2017) 106–115, https://doi.org/10.1016/j.electacta.2017.04.084.

[13] W. Cui, N. Cheng, Q. Liu, C. Ge, A.M. Asiri, X. Sun, High-efficient electrochemical hydrogen evolution catalyzed by Tungsten phosphide submicroparticles, ACS Catal. 4 (2014) 2658–2661.

[14] C. Wang, J. Jiang, T. Ding, G. Chen, W. Xu, Q. Yang, Monodisperse ternary NiCoP nanostructures as bifunctional electrocatalyst for hydrogen and oxygen evolution reactions with excellent performance, Adv. Mater. Interfaces 3 (2016) 1500454.

[15] T. Wang, H. Xie, M. Chen, A. D'Aloia, J. Cho, G. Wu, Q. Li, Precious metal-free approach to hydrogen electrocatalysis for energy conversion: From mechanism understanding to catalyst design, Nano Energy 42 (2017) 69–89, https://doi.org/10.1016/j.nanoen.2017.10.045.

[16] B.G. Pollet, The use of ultrasound for the fabrication of fuel cell materials, Int. J. Hydrogen Energy 35 (21) (2010) 11986–12004, https://doi.org/10.1016/j.ijhydene.2010.08.021.

[17] B.G. Pollet, A short introduction to sonoelectrochemistry, Electrochem. Soc. Interface 27 (3) (2018) 41–42, https://doi.org/10.1149/2.F03183if.

[18] Y. Sun, C. Wang, T. Ding, J. Zuo, Q. Yang, Fabrication of amorphus $CoMoS_4$ as a bifunctional electrocatalyst for water splitting under strong alkline conditions, Nanoscale 8 (2016) 18887–18892.

[19] X. Ren, D. Wu, R. Ge, X.u. Sun, H. Ma, T. Yan, Y. Zhang, B. Du, Q. Wei, L. Chen, Self-supported CoMoS4 nanosheet array as an efficient catalyst for hydrogen evolution reaction at neutral pH, Nano Res. 11 (4) (2018) 2024–2033, https://doi.org/10.1007/s12274-017-1818-6.

[20] (a) M. H. Islam, M. T.Y. Pual, O. S. Burheim, B. G. Pollet, Recent develoment in the sonochemical synthesis of nanomaterials, Ultrason. Sonochem. 59 (2019) 104711. (b) V. Zin, B.G. Pollet, M. Dabala, Sonoelectrochemical (20 kHz) production of platinum nanoparticles from aqueous solutions, Electrochim. Acta, 54 (2009) 7201-7206.

[21] (a) D.S. Karousos, K. I Desdenakis, P. M, Sakkas, G. Sourkouni, B. G. Pollet, C. Agirusis, Sonoelectrochemical one-pot synthesis of Pt- Carbon black nanocmposite PEMFC electrocatalyst, , Ultrason. Sonochem. 35 (2017) 591-597. (b) B. G. Pollet, The use of power ultrasound for the production of PEMFC and PEMWE catalysts and low-Pt loading and high-performing electrodes, Catalyst, 9 (2019) 246.

[22] A.A. Yadav, Y.M. Hunge, S.B. Kulkarni, C. Terashima, S.–W. Kang, Three-dimensional nanoflower-like hierarchical arry of multifunctional copper cpbltate electrode as efficient electrocatalyst for oxygen evolution reaction and energy storage application, J. Colloid Interface Sci., 526 (2020) 476–485.

[23] Y. Guo, J. Tang, J. Henzie, B. Jiang, W. Xia, T. Chen, Y. Bando, Y.-M. Kang, M. Shahriar, A. Hosain, Y. Sugahara, Y. Yamauchi, Mesoporous Iron- doped MoS_2/$CoMo_2S_4$ heterostructures through organic-metal cooperative intractions on spherical micelles for electrochemical water splitting, ACS Nano 14 (2020) 4141–4152.

[24] Y.Y. Ning, D. Ma, Y. Shen, F. Wang, X. Zhang, Tuning active sites on coblt/nitrogen doped graphene for electrocatalytic hydrogen and oxygen evolution, Electrochem. Acta 265 (2018) 18–31.

[25] Y.-K. Wang, W.-B. Zhang, Y. Zhao, K. Li, L.-B. Kong, Coprecipitation reaction system synthesis and lithium-ion capacitor energy storage application of the porous structural bimetallic sulfide $CoMoS_4$ nanopaticles, ACS Omega 3 (2018) 8803–8812.

[26] Q. Li, X.-Q. Qiao, Y. Jia, D. Hou, D.-S. Li, Amorphous $CoMoS_4$ nanostructure for photocatalytic H_2 generation, nitrophenol reduction, and methylene blue adsorption, ACS Appl. Nano Mater. 3 (1) (2020) 68–76, https://doi.org/10.1021/acsanm.9b01582.s001.

[27] Y.-H. Dai, L.-B. Kong, K. Yan, M. Shi, T. Zhang, Y.-C. Luo, L. Kang, Simple synthesis of a $CoMoS_4$ based nanostructure and its application for high-performance supercapacitors, RSC Adv. 6 (9) (2016) 7633–7642, https://doi.org/10.1039/C5RA26157K.

[28] J. Guo, X. Zhang, Y. Sun, L. Tang, X. Zhang, Self-template synthesis of hierarchical $CoMoS_3$ nanotubes constructed of ultrathin nanosheets for robust water electrolysis, J. Mater. Chem. A 5 (22) (2017) 11309–11315, https://doi.org/10.1039/C7TA02768K.

[29] A.A. Yadav, V.S. Kumbhar, S.J. Patil, N.R. Chodankar, C.D. Lokhande, Supercapacitive properties of chemically deposited La_2O_3 thin film, Ceram. Int. 42 (1) (2016) 2079–2084, https://doi.org/10.1016/j.ceramint.2015.09.098.

[30] X.-Q. Qiao, Z.-W. Zhang, Q.-H. Li, D.-F. Hou, Q.-C. Zhang, J. Zhang, D.-S. Li, P.-Y. Feng, X.-H. Bu, In situ synthesis of n-n Bi_2MoO_6 and Bi_2S_3 heterojunctions for highly efficient photocatalystic removal of Cr(v), J. Mater. Chem. A 6 (2018) 22580–22589.

[31] T. Shinagawa, A.T. Garcia-Esparza, K. Takanabe, Insight on Tafel slopes from a microkinetic analysis of aqueous electrocatalysis for energy conversion, Sci. Rep. 5 (2015) 13801.

[32] X. Zheng, J. Guo, Y. Shi, F. Xiong, W.-H. Zhang, T. Ma, C. Li, Low-cost and high-performance $CoMoS_4$ and $NiMoS_4$ counter electrodes for dye-sensitized solar cells, Chem. Commun. 49 (2013) 9645–9647.

[33] C. Ouyang, X. Wang, C. Wang, X. Zhang, J. Wu, Z. Ma, S. Dou, S. Wang, Hierarchically porous Ni_3S_2 nanorod array foam as highly efficient electrocatalyst for hydrogen evolution reaction and oxygen evolution reaction, Electrochim. Acta 174 (2015) 297–301.

[34] T. Liu, Q. Liu, A.M. Asiri, Y. Luo, X. Sun, An amorphus CoSe film behaves as an active and stable full water–splitting electrocatalyst under strongly alkaline conditions, Chem. Commun. 51 (2015) 16683–16686.

[35] L. Shao, X. Qian, X. Wang, H. Li, R. Yan, L. Hou, Low-cost and highly efficient $CoMoS_4$/$NiMoS_4$-based electrocatalyst for hydrogen evolution reactions over a wide pH range, Electrochim. Acta 213 (2016) 236–243.

[36] H. Jin, J. Wang, D. Su, Z. Wei, Z. Pang, Y. Wang, In situ cobalt–cobalt oxide/N-doped carbon hybrids as superior bifunctional electrocatalysts for hydrogen and oxygen evolution, J. Am. Chem. Soc. 137 (7) (2015) 2688–2694, https://doi.org/10.1021/ja5127165.

[37] C.C.L. McCrory, S. Jung, J.C. Peters, T.F. Jaramillo, Benchmarking heterogeneous electrocatalysts for the oxygen evolution reaction, J. Am. Chem. Soc. 135 (45) (2013) 16977–16987, https://doi.org/10.1021/ja407115p.

[38] C.G. Morales-Guio, L.-A. Stern, X. Hu, Nanostructured hydrotreating catalysts for electrochemical hydrogen evolution, Chem. Soc. Rev. 43 (18) (2014) 6555, https://doi.org/10.1039/C3CS60468C.

[39] P. Hu, Z. Jia, H. Che, W. Zhou, N. Liu, F. Li, J. Wang, Engineering hybrid $CoMoS_4$/Ni_3S_2 nanostructures as efficient bifunctional electrocatalyst for overall water splitting, J. Power Sources 416 (2019) 95–103, https://doi.org/10.1016/j.jpowsour.2019.01.090.

[40] X. Dai, K. Du, Z. Li, M. Liu, Y. Ma, H. Sun, X. Zhang, Y. Yang, Co-doped MoS_2 nanosheets with the dominant CoMoS phase coated on carbon as an excellent electrocatalyst for hydrogen evolution, ACS Appl. Mater. Interfaces 7 (49) (2015) 27242–27253, https://doi.org/10.1021/acsami.5b08420.s001.

[41] W. Zheng, M. Liu, L.Y.S. Lee, Best practices in using foam-type electrodes for electrocatalytic performance bemchmark, ACS Energy Lett. 5 (2020) 3260–3264.

[42] S. Hao, L. Chen, C. Yu, B. Yang, Z. Li, Y. Hou, L. Lei, X. Zhang, NiCoMo hydroxide nanosheet arrays synthesized via chloride corrosion for overall water splitting, ACS Energy Lett. 4 (4) (2019) 952–959, https://doi.org/10.1021/acsenergylett.9b00333.s001.

[43] J. Liu, J. Wang, B. Zhang, Y. Ruan, L. Lv, X. Ji, K. Xu, L. Miao, J. Jiang, Hierarchical $NiCo_2S_4$@NiFe LDH heterostructures supported on nickel foam for enhanced overall-water-splitting activity, ACS Appl. Mater. Interfaces 9 (18) (2017) 15364–15372, https://doi.org/10.1021/acsami.7b00019.s001.

[44] Y. Yang, C. Li, X. Ma, S. Li, X. Du, X. Hao, A. Abdula, G. Guan, One-dimensional $CoMoS_4$ nanorod arrays as an efficient electrocatalyst for hydrogen evolution reaction, J. alloy. Comp. 821 (2020), 153245.